Regular Article - Soft Matter

Efficient snap-through of spherical caps by applying a localized curvature stimulus

Lucia Stein-Montalvo[1,2] , Jeong-Ho Lee[1], Yi Yang[1,4], Melanie Landesberg[1,3], Harold S. Park[1], and Douglas P. Holmes[1,a]

[1] Department of Mechanical Engineering, Boston University, Boston, USA
[2] *Present address* Department of Civil and Environmental Engineering, Princeton University, Princeton, USA
[3] *Present address* Yale University, New Haven, USA
[4] *Present address* Harvard John A. Paulson School of Engineering and Applied Sciences, Harvard University, Cambridge, USA

Abstract

Abstract In bistable actuators and other engineered devices, a homogeneous stimulus (e.g., mechanical, chemical, thermal, or magnetic) is often applied to an entire shell to initiate a snap-through instability. In this work, we demonstrate that restricting the active area to the shell boundary allows for a large reduction in its size, thereby decreasing the energy input required to actuate the shell. To do so, we combine theory with 1D finite element simulations of spherical caps with a non-homogeneous distribution of stimulus-responsive material. We rely on the effective *curvature stimulus*, i.e., the natural curvature induced by the non-mechanical stimulus, which ensures that our results are entirely stimulus-agnostic. To validate our numerics and demonstrate this generality, we also perform two sets of experiments, wherein we use *residual swelling* of bilayer silicone elastomers—a process that mimics differential growth—as well as a magneto-elastomer to induce curvatures that cause snap-through. Our results elucidate the underlying mechanics, offering an intuitive route to optimal design for efficient snap-through.

1 Introduction

Following the lead of organisms like the Venus fly trap [1,2] and the hummingbird [3], which rely on fast, snapping motions to capture prey, engineers often use snap-through instability of shell structures for functionality in design. Snapping rapidly releases stored elastic energy and does not require a continuously applied stimulus to maintain an inverted shape in bistable structures. Thus, snap-through instability is a particularly attractive mechanism for e.g., robotic actuators or mechanical muscles [4,5], optical devices [6], and dynamic building façades [7]. Each relies on a combination of geometry-endowed bistability [8] and a snap-inducing stimulus to achieve its purpose. The stimulus can be mechanical—e.g., an indentation force [9], pressure [5], or torque from a child's hands inverting a jumping popper toy [10]—or non-mechanical, e.g., temperature [11], voltage [4], a magnetic field [12], or differential growth [13,14], swelling [15,16], or de-swelling [17]. An important connection between these wide-ranging stimuli is that each destabilizes a shell by generating a change in the shell's curvature relative to its original, stress-free curvature.

In particular, non-mechanical stimuli alter the stress-free reference state, producing spontaneous or *natural curvature*. A classic example is the bimetallic beam of Timoshenko, which curves as its two layers experience different expansive responses to an increasing thermal stimulus [18]. The natural curvature may be observed as the shape that a beam adopts when free of external constraints and exposed to a stimulus that causes this beam to bend. In plates or shells, however, the natural curvature is generally not achievable at all points. In such *non-Euclidean* [19] structures, geometric incompatibility leads to residual stresses and often complex reconfiguration [20,21]. Still, the relationship between a stimulus and the corresponding natural curvature it induces in a residually stressed structure can be discerned via simple experimental methods based on the bending deformation of an equivalent beam. Calibration can be performed as an independent experiment, or in a manner similar to the *opening angle method*, wherein an axial slice exposes stresses induced by differential growth in tubular biological structures like arteries [22]. Thus, natural curvature serves as useful "effective" stimulus, allowing for generalization of these many non-mechanical, curvature-inducing stimuli. This concept was recently formalized within a non-Euclidean theoretical framework based on Koiter shell

---

[a] e-mail: dpholmes@bu.edu (corresponding author)

theory, revealing that the *curvature stimulus* behaves like a mechanical potential [15,23]. With experiments and simulations, Pezzulla et al. [15] demonstrated that their curvature potential framework captures instabilities of spherical shells subjected to a homogeneously applied curvature stimulus.

Advanced functional devices actuated by homogeneous, curvature-inducing stimuli often require significant energy input, or have high material costs. Common commercially available dielectric elastomer (DE) films require up to $150\,\mathrm{V}\,\mu\mathrm{m}^{-1}$ for most applications, resulting in driving voltages in the kV range, and proportionally high energy consumption [24,25]. Using less of these smart materials can decrease both cost and the likelihood of device failure. This need has inspired custom production of ultrathin electroactive films via methods like pad-printing [26] or electrospraying [27]. Clearly, it is desirable to reduce these costs for DEs and other stimulus-responsive devices without requiring such efforts. We find that snap-through behavior may be preserved in spherical caps while the size of the active region—that is, the portion of the shell subjected to an arbitrary curvature-inducing stimulus—is significantly reduced.

In the present study, we extend the work of Pezzulla et al. [15] to show that when the active portion of a snapping shell is strategically placed, the magnitude of the stimulus need not increase, thus allowing for significantly reduced energy and material needs overall. We demonstrate this with 1D numerical simulations performed in COMSOL Multiphysics, wherein a curvature stimulus acts on a section of an otherwise passive shell. We validate our numerics with experiments, in which shells respond to different curvature-inducing stimuli—this also serves to demonstrate the generality of our findings. In one series of experiments, we rely on localized differential swelling of silicone elastomers, and in the second we use a magneto-active elastomer. Our numerical and experimental methods are described in Sect. 2. In Sect. 3, we present our results to answer the question: Is the active region more effective when placed in the bulk of the shell, or at the edge? Next, we ask: What is the ideal size of the active region? In other words, what is the smallest active region that preserves snap-through behavior, without requiring the magnitude of the stimulus to increase? In Sect. 4 we present a scaling solution for the ideal size of the active region, which we derive via energy minimization. These findings, which our data support, offer a mechanics-informed route to optimization. The underlying physics revealed prompt an additional examination of how the critical curvature scales with the active area in each configuration (Sect. 5), which adds rigor to the comparison presented earlier (in Sect. 3). We offer concluding remarks in Sect. 6.

2 Methods

In this work, we study spherical caps in two configurations: "active bulk" (Fig. 1a), and "active boundary" (Fig. 1b). We refer to the angular depth of the shell measured from the pole as θ. The angular extent of the active region is denoted by θ_{a}, and is measured either from the pole or from the end of the passive region for the active pole and edge configurations, respectively. The shell thickness is given by h and the radius of curvature by R. Below, we describe our numerical and experimental methods.

2.1 1D numerics

We performed finite element simulations in COMSOL Multiphysics 5.2. Following Refs. [15,23], and because our experiments (Sect. 2.2) confirm that the shells we study retain rotational symmetry at least up to the point of snapping, the energy is minimized in the 1D profile curve of the shell. A circular segment with radius of curvature $R \in [9.65, 45.25]$ mm represents the midline of a spherical cap with an angular depth $\theta \in [0.52, 1.14]$ rad measured from the pole. This corresponds to $\theta/\sqrt{h/R} \in [2.2, 9.6]$, which covers most the range where curvature-induced snap-through occurs for fully active shells [15]. As we discuss in Sect. 4, this parameter compares the depth of the shell to the characteristic size of its bending-dominated boundary layer, which becomes central to our analysis. The ratio $\theta_{\mathrm{a}}/\theta$ is between 0.3 and 1 for the data presented herein, because we did not observe snapping for shells with $\theta_{\mathrm{a}}/\theta < 0.3$. The shell thickness $h \in [0.5, 1.3]$ mm (so that $h/R \in [0.015, 0.135]$) enters in the energy. The material is linear, elastic, and isotropic, with Poisson's ratio $\nu \in [0.25, 0.5]$. The Young's Moduli E_{a} and E_{p} of the active and passive regions were set to either $E_{\mathrm{a}} = E_{\mathrm{p}} \in [0.1, 20]$ MPa, or $E_{\mathrm{a}}/E_{\mathrm{p}} \in [0.005, 200]$. Despite that we assume a homogeneous modulus (see Sect. 4), we observe no significant impact of the modulus on our results. This is expected, since the bistability of the shell depends only on geometry [8]. A Dirichlet boundary condition is applied to the endpoint at the pole, while the edge end remains free.

Our model relies on the theoretical framework recently introduced by Pezzulla et al. [15] and detailed further by Holmes et al. [23], which offers significant advantages for numerical energy minimization in the presence of non-mechanical stimuli. The authors demonstrate that in the absence of in-plane stretching of the middle surface, the curvature-inducing stimulus may be decoupled from Koiter's elastic energy and treated as a potential of the natural curvature κ. Thus, it is straightforward to selectively apply a curvature stimulus. The elastic energy ($\mathcal{U}_{\mathrm{el}}$ in the schematic in Fig. 1b) must be minimized over the entire body, while the curvature potential $\mathcal{P}_{\kappa} \sim \kappa$ contributes to the total energy only in the active region. To capture the sudden, nonlinear snap-through instability, we use a custom arc-length method to vary the curvature stimulus κ [15]. A com-
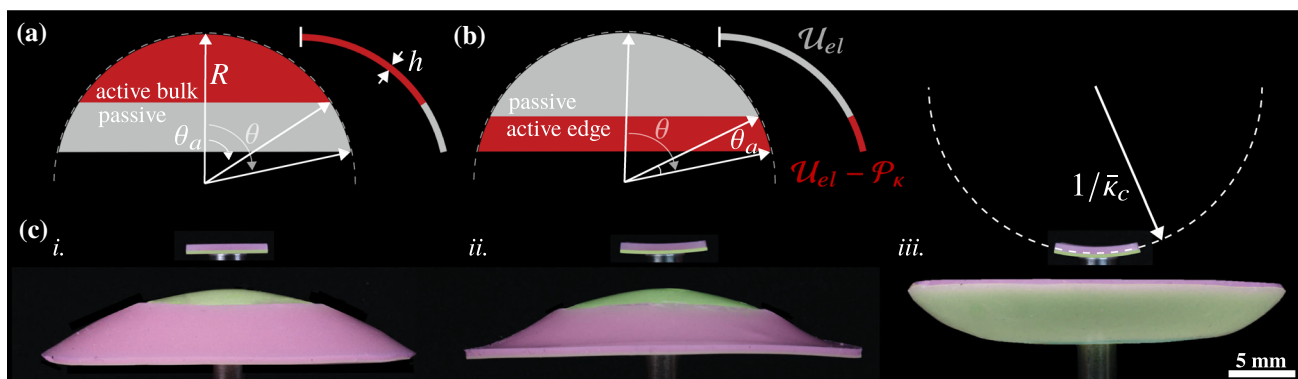
Fig. 1 Schematics of the **a** active bulk and **b** active edge configurations of the partially active spherical cap, with corresponding profile curves used in FEM simulations. Relevant parameters are labeled: the angular shell depth θ measured from the pole, the angular size of the active (red) region θ_a, and the radius of curvature R and thickness h. As depicted in **b**, the COMSOL model minimizes the elastic energy U_{el} over the whole body, with an additional contribution from the curvature potential $\mathcal{P}_\kappa$ in the active region. **c** Images from a typical residual swelling experiment in the active edge configuration. Residual swelling occurs in the bilayer (active) region, which has an outer pink layer (PVS 8) and an inner green one (PVS 32). Here, the pink layer contracts while the green layer beneath it expands, driving the curvature to increase. The beam has the same cross section as the bilayer region. Free from geometric constraints, it adopts the curvature $\bar{\kappa} = 1/R + \kappa$, revealing the evolving natural curvature stimulus κ that acts on the active region of the shell. The passive region consists of two (non-swelling) green layers. In i, the materials have just cured. ii The curvature stimulus creates a torque-like effect, causing the boundary of the shell to curl upward. The curvature evolves to a critical value $\bar{\kappa}_c$ when snap-through occurs, as shown in iii False color has been added to the thin, green layer of the beam, and to the inverted shell in iii

plete derivation of the equations used in COMSOL is provided in Ref. [23].

2.2 Experiments

To validate our numerical results, we performed experiments in which shells are made, in part, of stimulus-responsive elastomers. To emphasize the generality of the curvature stimulus, we did this in two ways. In one set of experiments, we used *residual swelling* of bilayer silicone elastomers [15,28–30], wherein diffusion of free polymer chains causes a geometric incompatibility resolved by curving. Deformation from residual swelling is growth-like and permanent. In additional experiments, we used magneto-active elastomers, which reversibly curve in response to a magnetic field. Below, we describe the methods used for each type of experiment.

2.3 Residual swelling experiments

It was previously demonstrated that residual swelling creates a curvature sufficient to drive inversion of full bilayer spherical caps [15]. In the present work, only a portion of the shell is subjected to residual swelling. Within this active region, we layer two polyvinylsiloxane (PVS) elastomers ($\nu = 0.5$), which we refer to as *green* (Zhermack Elite Double 32, E = 0.96 MPa) and *pink* (Zhermack Elite Double 8, E = 0.23 MPa). In a procedure detailed in "Appendix A" (see Fig. 6), we cast the materials one-by-one in their fluid state over a metal ball bearing to form a nominally green cap with either a bilayer ring at the edge, or a bilayer cap at the pole. In the active region, the outer layer is pink (see Fig. 1c). After cross-linking (which occurs in about 20 minutes at room temperature), the pink elastomer is left with residual, uncross-linked polymer chains. Thus, in the bilayer region where the pink and green material are in contact, there is a concentration gradient of free polymer chains. To resolve this, chains flow from the pink to the green elastomer. As such, the pink region loses mass, or shrinks, while the green region grows.

When this differential swelling occurs in a beam, the geometric mismatch between the length of the two layers, which are bonded together, results in a natural curvature—this is analogous to heating a bimetallic strip [18] or swelling a bilayer gel beam [31]. The beam is free to bend into the shape that minimizes its total potential energy, while remaining effectively stress-free. When applied instead to a plate or shell, the same stimulus attempts to bend the structure into a spherical surface. The curvature of this desired configuration is again referred to as the natural curvature. However, plates and shells must satisfy the Gauss–Codazzi–Mainardi compatibility equations. Bending into a sphere changes the Gaussian curvature, which cannot be accomplished without stretching the surface. This is energetically prohibitive for slender structures, so the natural curvature is not achieved everywhere, and a different configuration that is residually stressed is realized instead. Thus, while the magnitude of the natural curvature is essential for understanding the stable, equilibrium configurations of a structure, it cannot be readily determined or measured from the deformed shape. To determine the

natural curvature in our experiments, we must examine how a beam cut from the shell would deform.

To do so, we slice a small, bilayer beam from the same materials that make up the active region of the shell (see "Appendix A"; Fig. 6j), so that it has the same bilayer cross section. In our spherical caps, the bilayer region around the boundary curls upward (see Fig. 1c,ii), forming a lip like that which appears when a jumping popper toy is inverted [8,10]. Meanwhile, the free, unconfined beam adopts a curvature $\bar{\kappa}$, which is the sum of the initial curvature $-1/R$ and the natural curvature κ. Thus, the evolving, natural curvature stimulus is $\kappa = \bar{\kappa} + 1/R$ [15,28,29]. We mount the shell and beam side-by-side and use a Nikon D610 DSLR Camera to take time-lapse images at a rate of one photo per minute (maximum deformation is reached at about two hours post-cure.) The critical curvature κ_c is identified in ImageJ by fitting a circle to the beam in the image when snap-through occurs (see Fig. 1c,iii)—the radius of curvature is $1/\bar{\kappa}_c$. Residual swelling experiments produce curvatures up to $\kappa < \frac{1}{4h}$ [28,29]. Deep shells require higher curvatures for snap-through [15], so the geometric range accessed in experiments is limited compared to simulations. We performed experiments with $h/R \in [0.02, 0.07]$, $\theta \in [0.58, 0.98]$ rad, and $\theta_a/\theta \in [0.3, 1]$.

2.4 Magneto-elastomer experiments

The magneto-active shells are fabricated using a similar bilayer casting approach to the residual swelling shells. In this case, the ferromagnetic active layer consists of iron oxide (Fe_3O_4) nanoparticles (Sigma-Aldrich 637106) mixed with green PVS at a weight ratio of 20%. A passive PVS cap is made first, followed by a ferromagnetic edge ring. Then, an additional PVS layer is added to join the two, resulting in a shell of relatively uniform thickness with a passive bulk and active edge. We did not study the active bulk configuration with magneto-elastomer shells. A 25.4 mm cubic NdFeB magnet (N52 grade by SuperMagnetMan) is used to generate the magnetic gradient. The strength is measured by the magnetic flux density $\mathcal{B}$, using a magnetometer (PCE Instruments Inc). The relative permeability and remanence of the NdFeB magnet are 1.04 and 1.45, respectively, giving $\mathcal{B} = 0.562$ T at the surface center of the magnets.

We tested five magnetic shells with $h/R \in [0.02, 0.04]$, $\theta = 0.86$ rad, and an active boundary region such that $\theta_a/\theta \in [0.07, 1]$. The center of the magneto-active shell is mounted on a PVS column (diameter 4.5 mm) to support the shell when magnetic field is applied. The NdFeB magnet is mounted vertically on Instron 5943 with a 5N load cell, then quasi-statically approaches the shell at a rate of 0.1 mm/s using the software Bluehill3. When the magnet reaches a critical distance from the shell, the magnetic body force acting on the ferromagnetic edge triggers snapping. The critical displacement is retrieved from the force-displacement curve. In order to find the corresponding critical $\mathcal{B}$, we simulate the
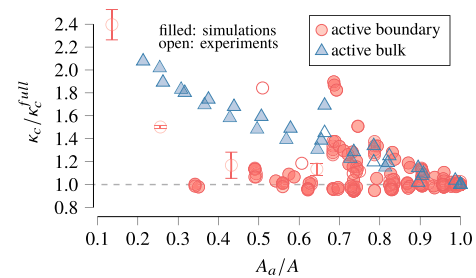
Fig. 2 Comparison of the critical curvature κ_c compared to that for a fully active shell, $\kappa_c^{full} = \kappa_c(\theta_a = \theta)$, for varied active area fraction, i.e., the active area compared to the total shell area, in the active bulk (blue triangles) and active boundary (pink circles) configurations. Our results show a clear preference for the active boundary configuration: A_a/A can be reduced to as low as about 0.34 without requiring a higher curvature stimulus for snap-through, whereas if the bulk is active (and the boundary is passive), $\kappa_c/\kappa_c^{full} > 1$ for any $A_a/A < 1$. Error bars correspond to one standard deviation, and are smaller than markers in all cases except the magneto-active experiments

magnetic field using the AC/DC module in COMSOL 5.6. This allows us to visualize the magnetic field and obtain $\mathcal{B}$ at given spatial points. Although the magnetic stimulus is non-homogeneous, we select the value of $\mathcal{B}$ at the edge of the shell for our analysis. To relate $\mathcal{B}$ to the curvature stimulus κ, we perform an additional set of experiments in which we measure the curvature in a ferromagnetic beam, oriented in the same direction as the edge of the shell, as the magnet approaches. For details on the magnetic field visualization and the magnetic flux-curvature calibration, see "Appendix B."

3 Comparison of active bulk and boundary

The total area of a spherical cap is $A = 2\pi R^2[1-\cos(\theta)]$. For the active bulk configuration, the active area $A_a = 2\pi R^2[1 - \cos(\theta_a)]$, and for shells with an active edge region, $A_a = 2\pi R^2[\cos(\theta - \theta_a) - \cos(\theta)]$. In Fig. 2, we compare the critical curvature κ_c to that for a fully active shell, $\kappa_c^{full} \equiv \kappa_c(\theta_a = \theta)$, for varied proportions of the active area to the total area of the shell, A_a/A—that is, $[1 - \cos(\theta_a)]/[1 - \cos(\theta)]$ for the active bulk and $[\cos(\theta - \theta_a) - \cos(\theta)]/[1 - \cos(\theta)]$ for the active edge configuration. In the active bulk configuration, a reduction of only 9 percent in A_a/A causes the critical curvature κ_c to increase significantly above κ_c^{full}. Meanwhile, we observe that when the boundary is active and the passive region lies in the bulk, the active portion can be reduced as much as 65 percent in some cases without requiring $\kappa_c/\kappa_c^{full} > 1$ for snap through.

As discussed in Sect. 2.1, it has been shown that a stimulus that induces intrinsic curvature may be treated as a *curvature potential*, which is decoupled from Koiter's elastic energy [15]. Pezzulla et al. demonstrate that this curvature potential may be further

decomposed into two work-like terms, one of which is integrated over the bulk of the shell, and the other around the boundary, i.e., $\mathcal{P}_\kappa = -\mathcal{W}_{\text{bulk}} - \mathcal{W}_{\text{edge}}$. Examining the two terms offers an interpretation of the non-mechanical curvature stimulus as analogous to combined mechanical loading: The bulk term has the form of an external pressure (mathematically, it is the normal displacement multiplied by the homogeneous natural curvature, which thus behaves as a hydrostatic pressure), whereas the edge term is torque-like (the dot product of a traction force and a rotation vector at the boundary). Furthermore, the authors present a scaling analysis to show that the normal, pressure-like term scales as:

$$\mathcal{W}_{\text{bulk}} \sim h^4 \kappa^2 (1 - \cos\theta), \tag{1}$$

and the torque-like term as:

$$\mathcal{W}_{\text{edge}} \sim h^4 \kappa^2 \left(\frac{R}{h}\right)^{3/2} \sin\theta. \tag{2}$$

Comparing the two contributions gives

$$\left|\frac{\mathcal{W}_{\text{edge}}}{\mathcal{W}_{\text{bulk}}}\right| \sim \frac{(R/h)^{3/2}}{\tan(\theta/2)} \gg 1, \tag{3}$$

showing that the edge work dominates in thin shells. In our experiments and simulations, as for those in Ref. [15], we observe that bulk deformation is negligible compared to boundary rotation in snapping, supporting this finding.

The implication explains our findings in general: removing a portion of active area from the edge weakens the effect of the curvature stimulus more than if the same amount of area were removed from the bulk, as bulk deformation due to the curvature stimulus is minimal to begin with. Conversely, the inequity suggests that the active edge configuration is the more efficient choice for the design of structures that will snap with minimal energy needs. To clearly distinguish between these regimes, henceforth we will refer to the critical curvature in the active boundary configuration as κ_c^{edge}, and that in the active bulk configuration as κ_c^{bulk}. Despite this clear preference for an active boundary, the optimal size of the active region is not clear from the scattered data in Fig. 2. We investigate this in the following section.

4 Optimal size of active boundary via energy minimization

To discern the most efficient size of the active region at the shell boundary, we minimize the total potential energy in the system $\mathcal{U}$, which consists of the internal elastic energy, and the non-mechanical loading due to curvature [14,15,23]. In the latter, the torque-like contribution at the boundary dominates over the pressure-like effect in the bulk. This effect is amplified in the

active edge configuration, as some or all of the bulk is passive. Accordingly, we observe very small bulk deformation compared to boundary rotation (see Fig. 5b) As such, we neglect the pressure-like contribution in the bulk. However, an additional torque-like effect arises at the boundary between the active and passive regions. This torque acts in the opposite direction to the one acting at the free boundary (see Fig. 3a), thus bending the two boundaries of the active region toward one another. Including this additional torque-like contribution at the active-passive interface gives:

$$\mathcal{U} = \mathcal{U}_{\text{K}} - \oint_{\text{out}} B(1+\nu)\kappa(\Delta\beta_{\text{out}})\, d\mathring{s}$$
$$- \oint_{\text{in}} B(1+\nu)\kappa(-\Delta\beta_{\text{in}})\, d\mathring{s} \tag{4}$$

where $\mathcal{U}_{\text{K}}$ is the Koiter shell energy [32], B is the bending rigidity, $\Delta\beta_{\text{out}}$ and $\Delta\beta_{\text{in}}$ are the angle change at the boundary and the active-passive interface, respectively, and $d\mathring{s}$ is the line element. The second and third terms quantify the torque-like contribution of the non-mechanical loading induced by the natural curvature at either end of the active edge region. Note that a positive angle change corresponds to a counter-clockwise rotation.

Because we expect axisymmetric deformation up to snap-through, these non-mechanical loading terms can be collected into the free boundary line integral as

$$\mathcal{U} = \mathcal{U}_{\text{K}} - \oint_{\text{out}} B(1+\nu)\kappa\Delta\beta_{\text{out}}^{\text{eq}}\, d\mathring{s} \tag{5}$$

where $\Delta\beta_{\text{out}}^{\text{eq}} = \Delta\beta_{\text{out}} - \Delta\beta_{\text{in}}\left(1 - \frac{\theta_a}{\theta}\right)$. Physically, this corresponds to transforming the shell into an equivalent one that experiences only the angle change $\Delta\beta_{\text{out}}^{\text{eq}}$ at the boundary, and is fully active, i.e., the natural curvature κ acts on the whole body (see Fig. 3b). Then, from Ref. [15], we can postulate that the snapping occurs when the colatitude-direction tangent vector at the boundary of the equivalent shell approximately becomes horizontal, i.e., at $\Delta\beta_{\text{out}}^{\text{eq}} \sim \theta$. Note that this does not imply that $\Delta\beta_{\text{out}} \sim \theta$, which as we discuss in Sect. 5, is not necessarily the case.

For thin surfaces where the non-mechanical stimulus acts through-the-thickness, the contribution of the mid-surface stretch induced by the stimulus can be neglected [15,23]. Then, assuming the colatitude-direction bending strain is much larger than the azimuthal one, the shell energy $\mathcal{U}$ scales as

$$\mathcal{U} \sim \frac{B}{2}\left(b_1^1\right)_p^2 A_p + \frac{B}{2}\left(b_1^1\right)_a^2 A_a$$
$$- B(1+\nu)\kappa\left[\Delta\beta_{\text{out}} - \Delta\beta_{\text{in}}\left(1 - \frac{\theta_a}{\theta}\right)\right](2\pi R\theta) \tag{6}$$

where b_1^1 is the characteristic curvature in the colatitude-direction and the subscripts p and a denote the passive bulk and active edge regions. The curvature

(a)

(b)
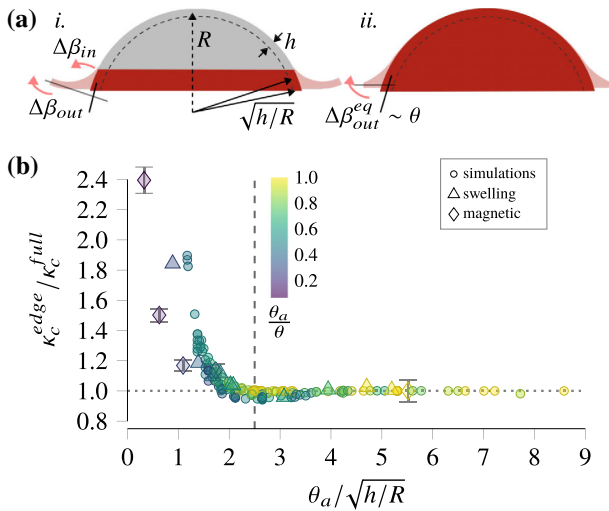
Fig. 3 a Schematic of the energy minimization scheme. The partially active shell is shown in *i*, where κ delivers a torque-like effect (pink arrows) along the free boundary and at the active-passive interface, which drives the tangent to the edge (black line) to rotate an amount $\Delta\beta_{\text{out}}$ (to the dark gray line) and that at the interface a smaller amount $\Delta\beta_{\text{in}}$. The characteristic angular size of the natural boundary layer, $\sqrt{h/R}$ is labeled. *ii* The equivalent fully active shell, which feels a torque from the curvature stimulus only about the free edge. Fully active shells snap-through when the tangent to the edge becomes approximately horizontal [15]. **b** The normalized critical curvature for the active edge configuration versus the active angular size θ_a compared to the characteristic angular scale of the natural boundary layer, $\sqrt{h/R}$. The data collapse supports the result Eq. (10), i.e., the optimal size for the active boundary region θ_a^* scales with the geometry-endowed boundary layer size

b_1^1 can be estimated as the angle change along an arc over its length, so that

$$(b_1^1)_{\text{p}} \sim \frac{-(\theta - \theta_{\text{a}} - \Delta\beta_{\text{in}})}{R(\theta - \theta_{\text{a}})} \qquad (7\text{a})$$

$$(b_1^1)_{\text{a}} \sim \frac{-(\theta_{\text{a}} + \Delta\beta_{\text{in}} - \Delta\beta_{\text{out}})}{R\theta_{\text{a}}}. \qquad (7\text{b})$$

The passive area A_{p} scales as $\pi R^2 \theta^2 - A_{\text{a}}$, and the active area A_{a} scales as $2\pi R^2 \theta \theta_{\text{a}}$. Inserting these scalings and minimizing Eq. (6) with respect to $\Delta\beta_{\text{in}}$ and $\Delta\beta_{\text{out}}$ gives the solutions for these rotations in the deformed configuration. Evaluating the result at the presumed point of instability, $\Delta\beta_{\text{out}}^{\text{eq}} \sim \theta$, gives the critical natural curvature of the partially active shell at snapping as:

$$\kappa_c^{\text{edge}} \sim \frac{\theta}{\theta_{\text{a}}(1+\nu)R}. \qquad (8)$$

Assuming the minimum critical curvature occurs at $\kappa_c = \kappa_c^{\text{full}}$, where from Ref. [15]:

$$\kappa_c^{\text{full}} \sim \frac{\theta}{(1+\nu)\sqrt{Rh}}, \qquad (9)$$

we find that the optimal size of θ_{a}, which we denote as θ_{a}^*, should scale as:

$$\theta_{\text{a}}^* \sim \sqrt{h/R}. \qquad (10)$$

We note that this corresponds to an optimal active area $A_{\text{a}}^* \sim 2\pi R^2[1 - \cos(\sqrt{h/R})]$, placed at the edge of the shell. The result in Eq. (10) is shown in Fig. 3b. We see a promising collapse of our data, and a minimum emerges at about 2.5 on the horizontal axis, indicating that the true optimal $\theta_{\text{a}}^* \approx 2.5\sqrt{h/R}$ for our shells, which vary in geometry, E, and ν. For moderately deep shells, we observe critical curvatures even below the predicted κ_c^{full} (as low as $\kappa_c = 0.95\kappa_c^{\text{full}}$, for a shell depth $\theta/\sqrt{h/R} = 5.3$ when $\theta_{\text{a}}/\theta = 0.5$). We suspect that this results from additional destabilizing effects delivered by the torque at the active-passive interface, which tends to help flatten the bulk of the shell. We note that magneto-elastomer shells carry more error than the residual swelling experiments and simulations. This is largely due to the non-uniform magnetic gradient generated from the NdFeB magnet. Additionally, the shells are highly sensitive to fabrication errors, which can result in a non-uniform ferromagnetic boundary.

The result of our energy minimization scheme given in Eq. (10) coincides with the angular scale of the bending-dominated *boundary layer* [33,34] for a spherical cap, $\sqrt{h/R}$. In open shells, the characteristic length of the boundary layer is that which is close enough to the edge that the thickness "feels" relatively large in comparison [35]. In this region, the energy balance shifts (thin shells are nominally stretching energy-dominated, preferring isometry), and so does the preferred deformation mode. The boundary layer is readily observed as the lip that curls upward when a spherical cap of finite thickness, e.g., a tennis ball sliced in half, is everted [8,36]. In this region, the shell "tries" to return to its initial state, resolving some of the stress that arises due to stretching above the midline and compression below it. Only if the boundary layer is large compared to the shell depth is the everted shell unstable, snapping back to its undeformed configuration. If the boundary layer is relatively small, the shell is bistable and can rest in its everted state indefinitely.

This scenario appears to be analogous to the non-everted, partially active shells we study: if the bending region is large, snap-through occurs easily, whereas a shell with a small active region is stable even against a higher stimulus. This points to an intuitive interpretation of our results: generally speaking, in the active edge configuration, if the angular size of the active region meets or exceeds that of the boundary layer θ_{bl}, the region predisposed to bending may do so. As a result,
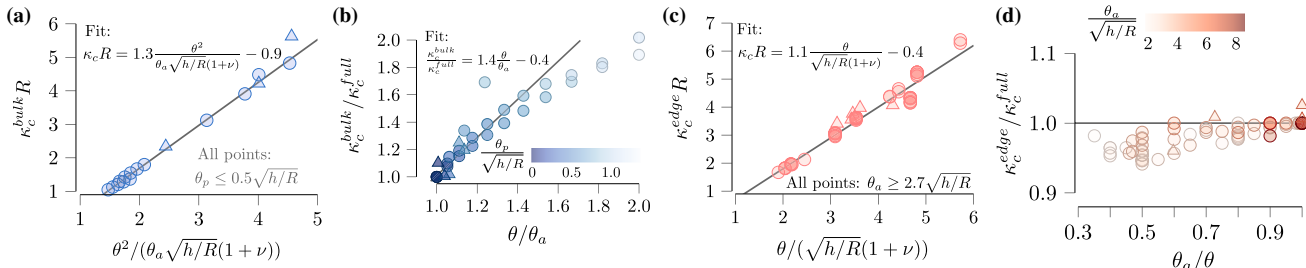
Fig. 4 a When the active portion of the shell is in the bulk, the size of the effective boundary layer is reduced. As a result, the critical curvature increases according to Eq. (12a), and any reduction in θ_a (greater than 1 on the x-axis) increases the curvature stimulus κ_c^{bulk} required for snap-through, as shown in **b**. As Eq. (12b) predicts, the stimulus increase scales linearly with θ/θ_a when the passive edge region is smaller than the boundary layer size (darker blue points, $\theta_p/\sqrt{h/R} \lesssim 0.5$; Fit corresponds to points in this range.) **c** If instead the boundary of the shell experiences the curvature stimulus, as long as θ_a exceeds the boundary layer, the behavior follows that of the fully active shell, i.e., Eq. (13a) [15] holds. **d** As such, θ_a can be reduced to as much as 0.35θ before the critical curvature increases above that for a fully active shell, κ_c^{full}, in agreement with Eq. (13b). In **a**–**d**, circular data points are from simulations, and triangles are from experiments

5 Scalings for the critical curvature based on fully active shells

In light of the importance of the boundary layer discussed in Sect. 4, we may add rigor to our claim that the active boundary configuration is more efficient than the active bulk (Sect. 3). To do so, we rely on the established result [15] (from which we determined Eq. (9)) that the critical curvature for fully active shells scales as:

$$\kappa_c^{\mathrm{full}} R \sim \frac{\theta}{(1+\nu)\sqrt{h/R}}. \tag{11}$$

This finding leans on the assumption that the pressure-like effect of curvature in the bulk may be neglected due to the dominant effect of curvature on the boundary, which we have similarly employed in Sect. 4. Additionally, it assumes based on empirical observations that the tangent vector to the boundary becomes approximately horizontal at the point of snap-through [14,15].

In the active bulk configuration, we reduce the size of the effective boundary layer. Accordingly, we observe that the tangent to the edge of the effective boundary

snapping is unaffected compared to a fully active cap. For $\theta_a < \theta_{\mathrm{bl}}$, we interfere with the boundary layer—this can be seen as reducing the size of the effective boundary layer—and higher curvatures are required to drive snap-through. The efficacy of the geometric design, in sum, depends on how the effective boundary layer set by θ_a, where we *impose* bending, relates to the natural boundary layer that scales as $\sqrt{h/R}$, where the shell *prefers* bending. In the active bulk configuration, any $\theta_a < \theta$ disturbs the boundary layer, forcing the critical curvature upward. Thus, this interpretation also clarifies what we saw in Sect. 3. This prompts us to briefly revisit our comparison of the active bulk and boundary configurations.
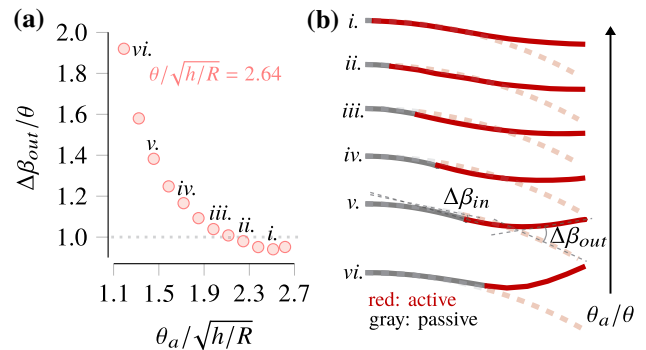

Fig. 5 a When the active region is large enough compared to the characteristic size of the boundary layer, the edge tangent requires a rotation $\Delta\beta_{\mathrm{out}} \sim \theta$ to snap through, which results in an approximately horizontal tangent. Data is from simulations of a fixed shell geometry with changing active area. For $\theta_a \lesssim 2\sqrt{h/R}$ in this case, the tangent undergoes additional rotation to trigger instability. Roman numerals correspond to **b**, which shows the initial (dashed) and immediately pre-snap (solid) profile curves for $\theta_a/\theta = 0.95, 0.85, \ldots, 0.45$. The rotations $\Delta\beta_{\mathrm{out}}$ and $\Delta\beta_{\mathrm{in}}$ are shown in v. The angle change $\Delta\beta_{\mathrm{out}}$ increases from 0.35 rad in i to 0.82 rad in vi

layer—that is, the active-passive interface, and not the edge of the shell—becomes approximately horizontal at the point of snap-through. Assuming the effective angular scale of the boundary layer scales as $(\theta_a/\theta)\sqrt{h/R}$, it follows from Eq. (11) that:

$$\kappa_c^{\mathrm{bulk}} R \sim \frac{\theta^2}{\theta_a(1+\nu)\sqrt{h/R}}, \qquad \theta_p < \theta_{\mathrm{bl}} \tag{12a}$$

$$\frac{\kappa_c^{\mathrm{bulk}}}{\kappa_c^{\mathrm{full}}} \sim \frac{\theta}{\theta_a}, \qquad \theta_p < \theta_{\mathrm{bl}}, \tag{12b}$$

where $\theta_{\mathrm{p}} = \theta - \theta_{\mathrm{a}}$ represents the passive portion of the shell. Eqs. (12a) and (12b) are shown in Fig. 4a&b, respectively, where indeed we see that the critical curvature increases linearly with $\theta/\theta_{\mathrm{a}}$ until the passive region reaches the approximate size of the boundary layer. At this point, where the entire boundary layer is inactive, the assumption that the edge work outweighs the bulk work breaks down and the critical curvature diverges.

For completeness, we also study the implications of Eq. (11) on shells with active boundaries. In Sect. 4, we used the horizontal tangent assumption ($\Delta\beta_{\mathrm{out}}^{\mathrm{eq}} \approx \theta$) for the equivalent fully active shell. We observe that for shells in the active edge configuration, this assumption breaks down, i.e., $\Delta\beta_{\mathrm{out}} > \theta$, if θ_{a} approaches the size of the boundary layer (see Fig. 5). With this in mind, as long as the coincident conditions that boundary layer is in tact and the boundary tangent is approximately horizontal at snap-through ($\theta_{\mathrm{a}} \gg \sqrt{h/R}$), due to the dominance of the edge work we expect no change to the critical curvature from $\kappa_{\mathrm{c}}^{\mathrm{full}}$. That is,

$$\kappa_{\mathrm{c}}^{\mathrm{edge}}R \sim \frac{\theta}{(1+\nu)\sqrt{h/R}}, \qquad \theta_{\mathrm{a}} > \theta_{\mathrm{bl}} \quad (13\mathrm{a})$$

$$\frac{\kappa_{\mathrm{c}}^{\mathrm{edge}}}{\kappa_{\mathrm{c}}^{\mathrm{full}}} = 1, \qquad \theta_{\mathrm{a}} > \theta_{\mathrm{bl}}. \quad (13\mathrm{b})$$

Note that Eq. (13b) is complementary to the result Eq. (8). Eqs. (13a) and (13b) are shown in Fig. 4c, d, respectively. Comparing Eqs. (12b) and (13b) confirms that for any small to moderate reduction to the active region, the active bulk configuration requires a higher curvature stimulus than the active boundary.

6 Conclusion

The aim of the present work was to guide the design of efficient snapping structures, which simultaneously minimize the active area and the magnitude of stimulus needed. We studied partially active spherical caps in two configurations—active bulk and active boundary—with a combination of theory, 1D finite element simulations, and experiments. Shells respond to a non-mechanical, curvature-inducing stimulus in the designated active region, but are passive elsewhere.

Our mechanics-informed approach uncovered an analogy to the bending-dominated boundary layer in inverted spherical caps. This offered an intuitive interpretation of our work: Selectively applying curvature amounts to setting the size of an effective boundary layer. Like for inverted, passive spherical caps, the size of the (effective) boundary layer is closely tied to stability [8]. Further, the location and size of the imposed bending region determines whether it competes against or cooperates with the geometric boundary layer, wherein the shell inherently "wants" to bend. With this view, the design principles that follow are straightforward. In the active cap configuration, some or all of the boundary layer is made passive, making

snap-through harder to achieve. As a result, the active edge configuration is preferred for efficient snapping. The angular size of the optimal active region scales with that of the natural boundary layer, $\sqrt{h/R}$ (Eq. (10)), with an empirical prefactor of about 2.5 for our shells.

We demonstrated the efficacy and generality of our findings using residually swelling and magneto-active shells. As we have shown, the curvature stimulus [15] may be mapped to a broad range of non-mechanical loads, so we expect that these principles will apply widely to bistable actuators. While the homogeneous curvature field assumed herein does not strictly apply to the magnetic stimulus, we found sufficient agreement with our experimental data. However, we expect that these and future results would be improved by more general theoretical framework that allows for a non-homogeneous curvature stimulus [37].

In our energy minimization scheme (Sect. 4), we assumed that the minimum curvature stimulus was that for the fully active shell. This allowed us to identify the optimal active angular size. However, we observed critical curvatures even below this value. We speculate that depending on the geometry, the torque at the active-passive interface can help to destabilize the shell—despite that it ostensibly acts in opposition to the edge torque. We leave investigation of this effect, which may open the door to further reduction of the critical curvature, for future work.

Author contribution statement

LSM carried out simulations, performed residual swelling experiments and data analysis, and wrote the manuscript. JHL developed the theory. YY carried out magneto-elastomer experiments. ML contributed to residual swelling experiments. HSP contributed to the theory. DPH conceived of the idea, supervised the study, contributed to the theory, and provided critical feedback on the manuscript.

Data Availability Statement This manuscript has associated data in a data repository. [Authors' comment: The datasets may be accessed at https://doi.org/10.5281/zenodo.5822440.]

A Fabrication of non-homogeneous residual swelling shells

The shell fabrication procedure for the active edge configuration is shown in Fig. 6. The process is as follows: To begin, we coat a metal ball-bearing ($R_{sphere} \in [12, 75]$ mm) with viscous polydimethylsiloxane (PDMS), ensuring a relatively uniform thickness [38]. Once the PDMS has cured, we use a laser-cut (Epilog Laser Helix, 75W) ring (inner radius $R_p \in [2, 65]$ mm) as a stencil to guide a circular cut, resulting in a cap of opening angle $\theta_p = \theta - \theta_a = \sin^{-1}(R_p/R_{sphere})$. Next, we coat a ball bearing of the same size with green polyvinylsiloxane (PVS) (Fig. 6a) and again make a cap with opening angle θ_p. This time, the cap remains in place and the excess material is removed (Fig. 6d). Since the active section necessarily has two layers of PVS, this additional passive layer ensures a relatively homogeneous thickness throughout the shell. With the green cap in place, a second layer of green PVS is added in the same manner (Fig. 6e) and cut to the edge angle, $\theta \geq \theta_p$. It fuses completely to the first layer, so in the bulk (the eventual passive region, up to θ_p) the material is thicker than at the edge at this stage of fabrication. After the second green PVS layer has cured, the PDMS cap is centered at the north pole (Fig. 6f). It adheres to but does not fuse with the PVS. Next, we deposit a layer of pink PVS (Fig. 6g). As soon as the pink layer is cured, a shallow cut is made around the edge of the PDMS cap (at θ_p) (Fig. 6h). Since the PDMS prevents cross-linking in the region it covers, we can peel the pink layer and the PDMS from this

section (Fig. 6i). Another laser cut ring ($R \in [6, 75]$ mm, $R > R_p$) is used to guide a deeper cut through both layers, forming the bottom boundary (Fig. 6j). This sets the total opening angle of the shell to be $\theta = \sin^{-1}(R/R_{sphere})$. We are left with a spherical cap composed of only green PVS (two layers thick) from opening angle 0 to θ_p, and a bilayer ring of angular size $\theta_a = \theta - \theta_p$ at the edge. In order to quantify the evolving curvature stimulus, we slice a small, vertical (initially curved) beam from the material that remains on the ball-bearing just below the cut (Fig. 6j). We mount the shell and beam side-by-side and use a Nikon D610 DSLR camera to take time-lapse images at a rate of one photo per minute. As residual swelling is a diffusive process, the time to deform scales with the square of the dimension across which swelling occurs [28]. In our experiments, that is the thickness h, and these shells reach maximum deformation by about two hours post-cure.

A shell with an active cap region is made in much the same way, except that the protective PDMS layer is a ring around the edge of the cap. This method prevents excision of a reliable bilayer beam from the region beneath the cut, so the curvature was not measured throughout the swelling process. Instead, a beam was cut from the cap region immediately following snapping, i.e., unlike in the active boundary configuration wherein we track the natural curvature throughout deformation, only the critical curvature κ_c is obtained for these experiments. Because the curvature develops at a much slower rate than that of snapthrough, the difference between the curvature immediately before and after snapping is negligible.
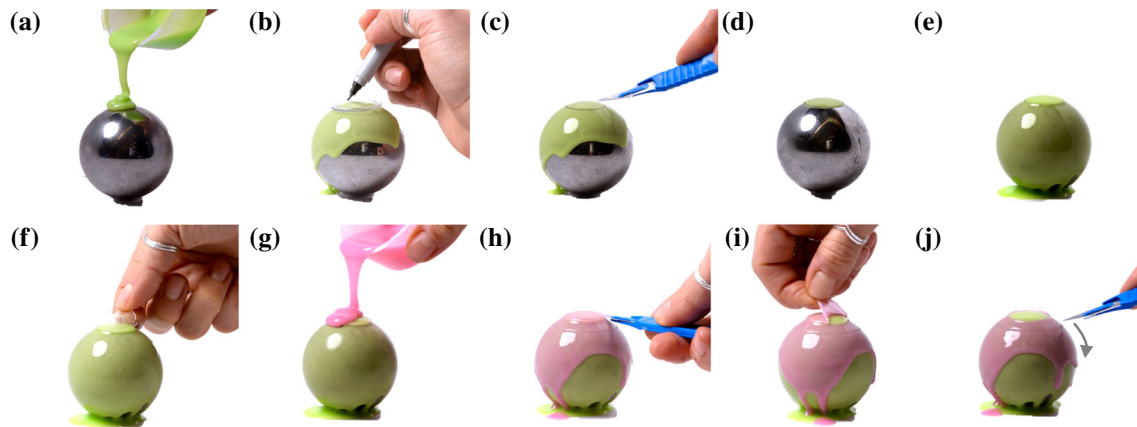

Fig. 6 The fabrication process for a non-homogeneous spherical cap with active edge: **a** A layer of viscous green PVS is deposited over spherical metal ball-bearing. **b** After curing, a ring of radius R_p is centered at the top of the sphere and used as a stencil to mark θ_p. **c** A cut is made and d. excess material is removed, leaving a green layer of angular size $0 \leq \theta \leq \theta_p$. **e** A second green layer is added. f. Once the green layer is cured, a PDMS cap (cut from a sphere of the same size, in the same manner as **a**–**d**) of radius R_p is centered at the top of the sphere. **g** A pink layer of PVS is added. After curing, a shallow cut **h** allows for the removal **i** of the pink layer and the PDMS in the region $0 \leq \theta \leq \theta_p$. **j** A cut is made at θ (following a line which was stenciled by a ring as in **b**) through all material to free the shell from the ball bearing. Finally, a small beam is cut vertically from just below the shell (in the direction of the gray arrow)

B Magnetic flux density as a curvature stimulus

In order to visualize the magnetic field and obtain the magnetic flux density $\mathcal{B}$ at given spatial points, we simulate the magnetic field using the AC/DC module in COMSOL 5.6 (see Fig. 7). The finite element model is calibrated with experimental measurements and material properties provided by the manufacturer. The critical $\mathcal{B} = \mathcal{B}_c$ at the edge of the shell at the point of snapping was calculated by inputting the critical displacement (measured from the Instron experiments) to the FE simulation.

To obtain the relationship between the applied magnetic flux density and corresponding natural curvature of the shell, we fabricated a beam of length 6.1 mm, width 0.88 mm, and thickness $h = 0.42$ mm. The beam is cut from the same spherical ball-bearing as the shells, so the initial curvatures are equivalent ($1/R = 0.0787$ mm^{-1}). The arch is oriented at 0.639 rad with respect to the vertical centerline to match the position of the corresponding ferromagnetic layer in the magnetic field (see Fig. 7c, d.) The magnetic field is generated using the same cubic NdFeB magnet as is used for the shell. Digital image processing is used to measure the change of curvature as we vary the distance between the magnet and the bottom edge of the beam. The distance is then converted to magnetic flux density $\mathcal{B}$ using the COMSOL FE simulation. The response curvature as a function of the applied magnetic flux density over the range relevant to our experiments is shown in Fig. 7b. In our range, a first order polynomial fits the data. We note that the intercept of our empirical fit, which has a slope of 0.097, is not zero, indicating that a linear fit would not be sufficient over a larger range.
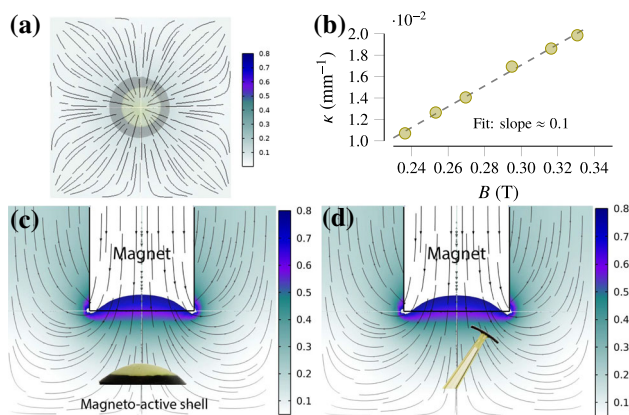
Fig. 7 **a** Finite element simulation showing the axially symmetric magnetic field generated from the NdFeB magnet. **b** Calibration curve for magnetic flux density $\mathcal{B}$ versus the curvature stimulus κ, based on measurements taken from the beam in **d**. **c** Magneto-active shell in the magnetic field. **d** Magneto-active beam the magnetic field, which is oriented to match the edge of the shell and used to calibrate the κ–$\mathcal{B}$ relationship. In our range, the relationship is approximately linear, and for our shells, we used the empirical fit indicated by the dashed line

References

1. Y. Forterre, J.M. Skotheim, J. Dumais, L. Mahadevan, Nature **433**(7024), 421 (2005). https://doi.org/10.1038/nature03185
2. R. Sachse, A. Westermeier, M. Mylo, J. Nadasdi, M. Bischoff, T. Speck, S. Poppinga, Proc. Natl. Acad. Sci. **117**(27), 16035 (2020). https://doi.org/10.1073/pnas.2002707117
3. M. Smith, G. Yanega, A. Ruina, J. Theor. Biol. **282**(1), 41 (2011). https://doi.org/10.1016/j.jtbi.2011.05.007
4. H. Shao, S. Wei, X. Jiang, D.P. Holmes, T.K. Ghosh, Adv. Func. Mater. **28**(35), 1802999 (2018). https://doi.org/10.1002/adfm.201802999
5. B. Gorissen, D. Melancon, N. Vasios, M. Torbati, K. Bertoldi, Sci. Robot. **5**(42), eabb1967 (2020). https://doi.org/10.1126/scirobotics.abb1967
6. D. Holmes, A. Crosby, Adv. Mater. **19**(21), 3589 (2007). https://doi.org/10.1002/adma.200700584
7. J.Y. Song, S. Heo, J. Shim, Technol. Architect. Des. **2**(1), 45 (2018). https://doi.org/10.1080/24751448.2018.1420964
8. M. Taffetani, X. Jiang, D.P. Holmes, D. Vella, Proc. R. Soc. A **474**(2213), 20170910 (2018). https://doi.org/10.1098/rspa.2017.0910
9. G. Wan, Y. Cai, Y. Liu, C. Jin, D. Wang, S. Huang, N. Hu, J.X. Zhang, Z. Chen, Extreme Mech. Lett. **42**, 101065 (2021). https://doi.org/10.1016/j.eml.2020.101065
10. A. Pandey, D.E. Moulton, D. Vella, D.P. Holmes, Europhys. Lett. **105**(2), 24001 (2014). https://doi.org/10.1209/0295-5075/105/24001
11. M. Jakomin, F. Kosel, T. Kosel, Thin-Walled Struct. **48**(3), 243 (2010). https://doi.org/10.1016/j.tws.2009.10.005
12. K.A. Seffen, S. Vidoli, Smart Mater. Struct. **25**(6), 065010 (2016). https://doi.org/10.1088/0964-1726/25/6/065010
13. A. Goriely, *The Mathematics and Mechanics of Biological Growth* (Springer, Berlin, 2017)
14. J.H. Lee, H.S. Park, D.P. Holmes, Phys. Rev. Lett. **127**(13), 138102 (2021). https://doi.org/10.1103/physrevlett.127.138102
15. M. Pezzulla, N. Stoop, M.P. Steranka, A.J. Bade, D.P. Holmes, Phys. Rev. Lett. **120**, 048002 (2018). https://doi.org/10.1103/PhysRevLett.120.048002
16. A.M. Abdullah, P.V. Braun, K.J. Hsia, Soft Matter **12**(29), 6184 (2016). https://doi.org/10.1039/c6sm00532b
17. Y. Kim, J. van den Berg, A.J. Crosby, Nat. Mater. **20**, 1695–1701 (2021). https://doi.org/10.1038/s41563-020-00909-w
18. S. Timoshenko, J. Opt. Soc. Am. **11**(3), 233 (1925). https://doi.org/10.1364/JOSA.11.000233
19. E. Efrati, E. Sharon, R. Kupferman, J. Mech. Phys. Solids **57**(4), 762 (2009). https://doi.org/10.1016/j.jmps.2008.12.004
20. Y. Klein, E. Efrati, E. Sharon, Science **315**(5815), 1116 (2007). https://doi.org/10.1126/science.1135994
21. E. Sharon, E. Efrati, Soft Matter **6**(22), 5693 (2010). https://doi.org/10.1039/c0sm00479k
22. V. Alastrué, E. Peña, M.Á. Martínez, M. Doblaré, Ann. Biomed. Eng. **35**(10), 1821 (2007). https://doi.org/10.1007/s10439-007-9352-4

23. D.P. Holmes, J.H. Lee, H.S. Park, M. Pezzulla, Phys. Rev. E **102**(2), 023003 (2020). https://doi.org/10.1103/physreve.102.023003

24. A. O'Halloran, F. O'Malley, P. McHugh, J. Appl. Phys. **104**(7), 071101 (2008). https://doi.org/10.1063/1.2981642

25. T. Lu, C. Ma, T. Wang, Extreme Mech. Lett. **38**, 100752 (2020). https://doi.org/10.1016/j.eml.2020.100752

26. A. Poulin, S. Rosset, H.R. Shea, Appl. Phys. Lett. **107**(24), 244104 (2015). https://doi.org/10.1063/1.4937735

27. F.M. Weiss, T. Töpper, B. Osmani, S. Peters, G. Kovacs, B. Müller, Adv. Electron. Mater. **2**(5), 1500476 (2016). https://doi.org/10.1002/aelm.201500476

28. M. Pezzulla, S.A. Shillig, P. Nardinocchi, D.P. Holmes, Soft Matter **11**(29), 5812 (2015). https://doi.org/10.1039/C5SM00863H

29. M. Pezzulla, G.P. Smith, P. Nardinocchi, D.P. Holmes, Soft Matter **12**, 4435 (2016). https://doi.org/10.1039/C6SM00246C

30. L. Stein-Montalvo, P. Costa, M. Pezzulla, D.P. Holmes, Soft Matter **15**(6), 1215 (2019). https://doi.org/10.1039/C8SM02035C

31. A. Lucantonio, P. Nardinocchi, M. Pezzulla, Proc. R. Soc. A **470**(2171), 20140467 (2014). https://doi.org/10.1098/rspa.2014.0467

32. W.T. Koiter, J.G. Simmonds, *Theoretical and Applied Mechanics* (Springer, Berlin, 1973), pp. 150–176

33. Y.C. Fung, W.H. Wittrick, Q. J. Mech. Appl. Math. **8**(2), 191 (1955). https://doi.org/10.1093/qjmam/8.2.191

34. F. Niordson, *Shell Theory* (Elsevier Science, Amsterdam, 1985)

35. E. Efrati, E. Sharon, R. Kupferman, Phys. Rev. E **80**(1), 016602 (2009). https://doi.org/10.1103/physreve.80.016602

36. D.P. Holmes, Curr. Opin. Colloid Interface Sci. **40**, 118 (2019). https://doi.org/10.1016/j.cocis.2019.02.008

37. J.H. Lee, H.S. Park, D.P. Holmes, Forthcoming (2022)

38. A. Lee, P.T. Brun, J. Marthelot, G. Balestra, F. Gallaire, P.M. Reis, Nat. Commun. **7**(1), 1–7 (2016). https://doi.org/10.1038/ncomms11155